**OPEN**

# Fracture mode control: a bio-inspired strategy to combat catastrophic damage

Haimin Yao[1], Zhaoqian Xie[1], Chong He[1] & Ming Dao[2]

[1]Department of Mechanical Engineering, the Hong Kong Polytechnic University, Hung Hom, Kowloon, Hong Kong SAR, China, [2]Department of Materials Science and Engineering, Massachusetts Institute of Technology, Cambridge, MA 02139, USA.

The excellent mechanical properties of natural biomaterials have attracted intense attention from researchers with focus on the strengthening and toughening mechanisms. Nevertheless, no material is unconquerable under sufficiently high load. If fracture is unavoidable, constraining the damage scope turns to be a practical way to preserve the integrity of the whole structure. Recent studies on biomaterials have revealed that many structural biomaterials tend to be fractured, under sufficiently high indentation load, through ring cracking which is more localized and hence less destructive compared to the radial one. Inspired by this observation, here we explore the factors affecting the fracture mode of structural biomaterials idealized as laminated materials. Our results suggest that fracture mode of laminated materials depends on the coating/substrate modulus mismatch and the indenter size. A map of fracture mode is developed, showing a critical modulus mismatch (CMM), below which ring cracking dominates irrespective of the indenter size. Many structural biomaterials in nature are found to have modulus mismatch close to the CMM. Our results not only shed light on the mechanics of inclination to ring cracking exhibited by structural biomaterials but are of great value to the design of laminated structures with better persistence of structural integrity.

Biological competition between predator and prey happens ubiquitously in nature. Through millions of years' evolution, organisms have developed diverse strategies to enhance their chance of survival. For example, animals such as fishes, turtles and snails, tend to equip themselves with hard exoskeletons to protect their vulnerable bodies. The survival of these species through biological competitions proved the success of the adopted biological materials in protection against the mechanical attacks and may imply ingenious design conceptions potentially applicable to the synthetic protective materials in engineering. In recent decades, intensive efforts[1–4] have been devoted to the studies on bioarmors in an attempt to understand the underlying principles for material design. So far, most works have been focusing on the mechanisms accounting for the excellent mechanical properties such as higher strength and toughness compared to their building constituents[5–13], inspiring a number of biomimetic endeavors[14–17]. Despite the strengthening and toughening mechanisms which increase the difficulty of crack formation and propagation in materials, fracture is still unavoidable when overwhelming loading is encountered. Under this circumstance, reducing the scope of damage to the minimum extent becomes a realistic choice to combat the catastrophic damage which is vital to the survival of the individuals and even the species. Such strategy is believed to be present in nature after reviewing the findings of recent studies on structural biomaterials. For instance, it has been reported that indentation on the scale of *Polypterus senegalus*, a 'living-fossil' fish species, normally causes ring cracks rather than radial ones[1]. Such inclination to ring cracks was also exhibited by the shell of *Crysomallon squamiferum*[18], a snail species inhabiting in deep sea hydrothermal environment, and teeth of *Mylopharyngodon piceus* (see Fig. 1a), a fish species feeding on mollusks[19]; but it is not often the case in synthetic systems such as glass coating on polymeric substrate[20] (Fig. 1b) and dental crown[21]. From the perspective of overall structural integrity, ring cracks are more localized and therefore less destructive than the radial ones. Is the inclination to ring cracking exhibited by the above-mentioned biological structural materials an accidental phenomenon or a consequence of evolution? If it results from natural selection, what are the geometrical and mechanical features of the structural materials that regulate their fracture modes under indentation? Are there any guidelines that we can follow to control the fracture modes as desired? Speculation of these questions inspires us to investigate the mechanics of fracture modes of biological materials undergoing external load represented by indentation.

For a material free of pre-existing defects, fracture due to external loadings tends to start from crack initiation, followed by crack propagation. The location of the crack initiation and the orientation of the resulting crack plane depend on the stress field developed by the external loading, and the anisotropy, inhomogeneity and "mechanical
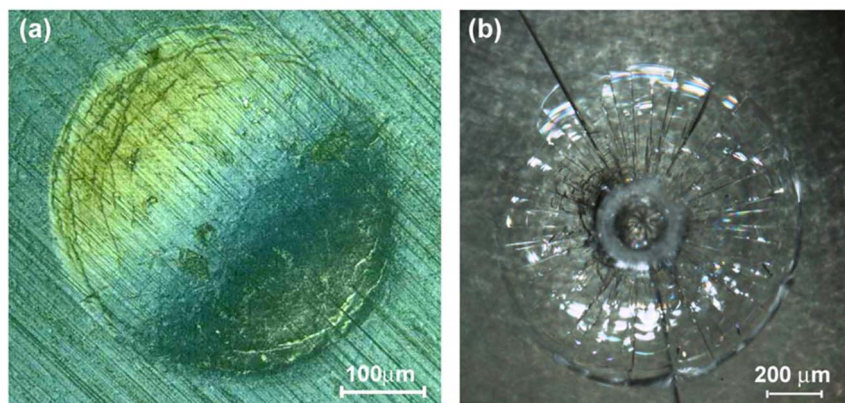
**Figure 1** | (a) Ring cracks created by indentation on the occlusal surface of a black carp tooth. (b) Radial cracks produced by indentation on a glass coating attached on epoxy substrate.

nature" of the material. For example, a homogeneous and isotropic cylinder specimen, when subjected to uniaxial tension, generally breaks along the plane perpendicular to the longitudinal axis if it is made by brittle material while fractures along conical surface at 45° to the longitudinal axis if it is made by ductile material. This is because brittle materials generally fail along the plane with maximum tensile stress while the ductile materials often fail along the plane having maximum shear stress. To predict the onset of crack initiation as well as the orientation of the resulting crack plane, setting a proper failure criterion is necessary. Due to the lack of a universal failure criterion, various failure criteria have been developed for materials with diverse mechanical natures[22]. For example, the simple maximum-tensile-stress criterion, also known as Rankine criterion[23], states that a crack forms when the maximum tensile principal stress ($\sigma_1$) exceeds the fracture strength ($\sigma_f$) of the material. It applies to brittle and even quasi-brittle materials such as concrete, rocks, minerals and ceramics if the materials' anisotropy and inheterogeneity are negligible. The plane of the resulting crack predicted by the Rankine criterion is perpendicular to the direction of the maximum principal stress. Considering that most structural biomaterials are biomineralized composites with brittle minerals (e.g. calcium carbonate and hydroxyapatite) being their major constituents, Rankine criterion[23] is considered suitable for them.

Most structural biomaterials in nature exhibit laminated microstructures. For example, the shell of *Crysomallon squamiferum* consists of a compliant organic layer sandwiched by the outer iron sulfide layer and inner calcium carbonate layer[18]; the scale of *Polypterus senegalus* comprises four layers including ganoine, dentine, isopedine and bone[1]; the tooth of *Mylopharyngodon piceus* is composed of enameloid and dentine layers[19]. Although these laminated structures display great diversity, common features in structure and mechanical property are still present. For example, the most outer layer in these structures is found to be notably stiffer and thinner than the adjacent layer. We thus speculate that the fracture modes of laminated structures may depend on the layout of thicknesses and mechanical properties in different layers. To shed light on the factors affecting the fracture modes, theoretical modeling is carried out within the framework of contact mechanics.

## Results

**Theoretical modeling.** Consider an idealized bilayer structure consisting of an elastic coating firmly attached on an elastic substrate, as shown in Fig. 2a. The elastic moduli and Poisson's ratios of the coating and substrate are denoted by $E_c$, $E_s$, $v_c$ and $v_s$, respectively. Although structural biomaterials in nature often consist of layers more than two, this simplified bilayer model is still applicable considering that the most outer layer is normally much thinner than the adjacent layer. A rigid (non-deformable) spherical indenter is compressed by force $P$ onto the laminated structure, simulating the external attack from, for example, predators. Friction between the indenter and coating is neglected. Following the convention in contact mechanics, the profile of the spherical indenter is approximated by a paraboloid of revolution described by $f(r) = r^2/2R$ (see Fig. 2a), where $R$ is the tip radius characterizing the dimension of the indenter. According to the Rankine criterion, the prediction of fracture modes entails the knowledge of the maximum principal stress $\sigma_1$ especially its peak value(s) and location(s) of emergence.

**Evolution of the maximum stress.** The contact problem posed above has been extensively studied in literature[24–28]. Previous results indicated two possible locations of the maximum principal stress $\sigma_1$ on the coating surface ($z = 0$) and the axis of symmetry ($r = 0$) respectively, as illustrated in Fig. 2b, c. In both cases, $\sigma_1$ was found to be along the radial direction. Therefore, these two local peaks of $\sigma_1$ represent the maximum radial stresses on the coating surface (CS) and along the axis of symmetry (AoS) respectively. The existence of two local peaks of $\sigma_1$ on CS and AoS has also been reported in materials with continuously graded Young's modulus[29,30]. In particular, for materials with exponentially graded Young's modulus[29] along the depth direction, $E \propto e^{\alpha z}$, the maximum of $\sigma_1$ occurs at the contact perimeter when $\alpha > 0$ while below the surface along the $z$-axis when $\alpha < 0$.

It can be shown that (Supplementary Information) the radial stress components in the coating can be expressed as $\frac{E_c^* t}{\pi R} \bar{\sigma}(\bar{r}, \bar{z}, \bar{a}, \frac{E_c}{E_s}, v_c, v_s)$, where $E_c^* = \frac{E_c}{1 - v_c^2}$ is the reduced modulus of coating, $t$ denotes the thickness of the coating, normalized radial stress $\bar{\sigma}(\cdot)$ is a dimensionless function of the normalized coordinates $\bar{r} = \frac{r}{t}$, $\bar{z} = \frac{z}{t}$ and four non-dimensional parameters including the normalized contact radius $\bar{a} = \frac{a}{t}$, modulus ratio $E_c/E_s$, Poisson's ratios $v_c$ and $v_s$. Given these four non-dimensional parameters, the normalized maximum principal stress $\bar{\sigma}_1 \equiv \sigma_1 \pi R / E_c^* t$ can be obtained semi-analytically for any point with normalized coordinates $\bar{r}$ and $\bar{z}$(Supplementary Information). For example, taking $E_c/E_s = 4.0$, $v_c = v_s = 0.3$, the calculated distributions of $\bar{\sigma}_1$ along AoS ($r = 0$) and CS ($z = 0$) at different contact radii are shown in Fig. 3a and b, respectively. It can be seen that the maximum principal stress along the AoS increases monotonically from compressive to tensile as the depth $z$ increases. It reaches the peak value, denoted by $\left(\sigma_1^{AoS}\right)_{pk}$, at the coating/substrate interface ($z = t$). In contrast, on the CS the location of the peak $\sigma_1$ is not fixed but changes with the contact radius. Fig. 3b shows that the peak $\sigma_1$ on the CS occurs
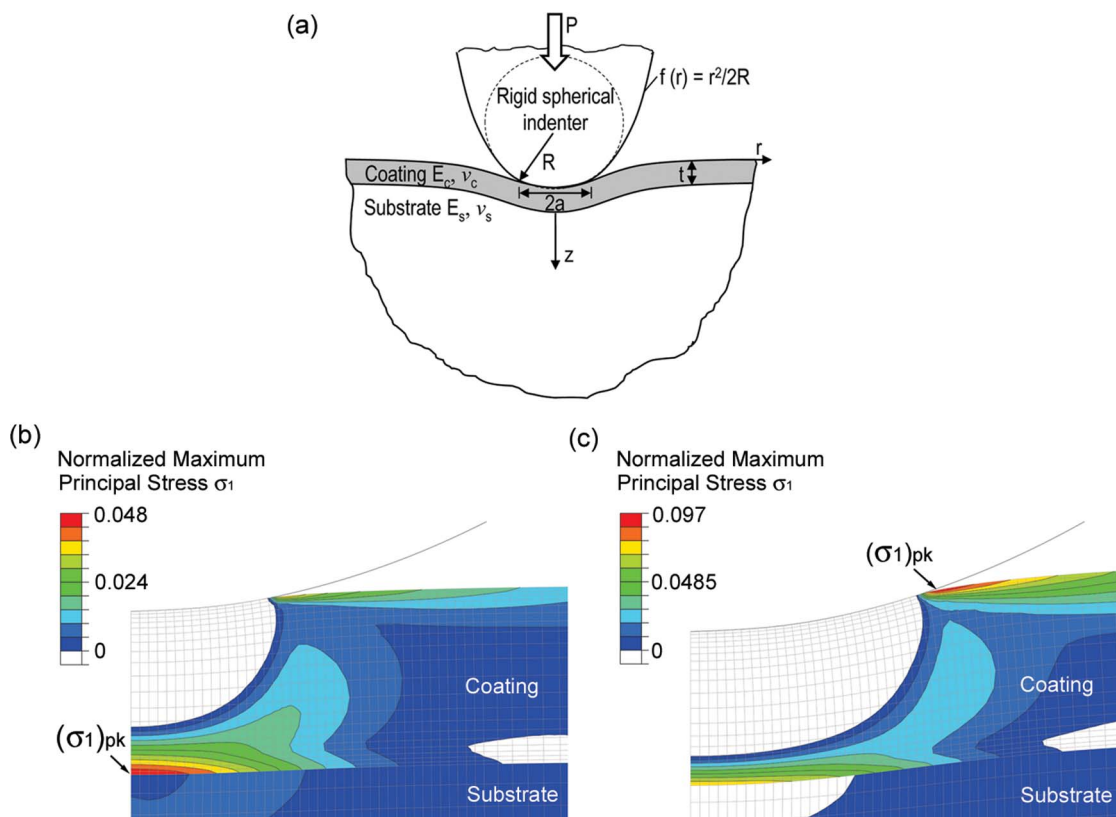
**Figure 2** | (a) Schematic of an elastic coating/substrate structure under indentation by a rigid indenter. The peak value of the maximum tensile principal stress, $(\sigma_1)_{pk}$, for the contact problem in (a) may occur at two possible positions. One is along the axis of symmetry at the coating/substrate interface as shown in (b), and another one is on the coating surface near the contact perimeter as shown in (c). Here normalized maximum principal stress is defined as $\bar{\sigma}_1 \equiv \sigma_1 \pi R / E_c^* t$.

exactly at the contact perimeter ($r = a$, $z = 0$) when the contact radius $a$ is relatively small in comparison with the coating thickness $t$. With the increase of contact radius $a$, the $\sigma_1$ at the contact perimeter decreases while that outside the contact region rises and finally exceeds the former. The peak value of $\sigma_1$ on the CS, no matter where it occurs, is denoted by $(\sigma_1^{CS})_{pk}$.

As indicated by Rankine criterion[23], cracking takes place if the maximum tensile principal stress $\sigma_1$ reaches the fracture strength $\sigma_f$ of the material. The presence of two local peaks of $\sigma_1$ under indentation implies two possible fracture modes. If $(\sigma_1^{CS})_{pk}$ reaches $\sigma_f$ first, ring cracking would happen as the plane of the resulting crack should be perpendicular to the direction of the $(\sigma_1^{CS})_{pk}$ which is along the radial direction. Otherwise, radial cracking would be initiated first as the crack should be on the plane passing through the AoS. The determination of the initial fracture mode entails the comparison between $(\sigma_1^{CS})_{pk}$ and $(\sigma_1^{AoS})_{pk}$. Fig. 4a shows the evolution of $(\sigma_1^{CS})_{pk}$ and $(\sigma_1^{AoS})_{pk}$ as functions of normalized contact radius when $E_c/E_s = 4.0$ and $\nu_c = \nu_s = 0.3$. It can be seen that at small contact size, $(\sigma_1^{CS})_{pk}$ is greater than $(\sigma_1^{AoS})_{pk}$. As indentation proceeds and contact radius increases, $(\sigma_1^{AoS})_{pk}$ exceeds $(\sigma_1^{CS})_{pk}$. But the predominance of $(\sigma_1^{AoS})_{pk}$ over $(\sigma_1^{CS})_{pk}$ is not lasting. With further increase of the contact radius, $(\sigma_1^{AoS})_{pk}$ would not increase all the way. Instead, there is a critical contact radius, at which $(\sigma_1^{AoS})_{pk}$ reaches its maximum and then decreases. After certain contact radius, $(\sigma_1^{AoS})_{pk}$ is surpassed by $(\sigma_1^{CS})_{pk}$. Since the fracture mode of the coating depends on whether $(\sigma_1^{AoS})_{pk}$ or $(\sigma_1^{CS})_{pk}$ reaches fracture strength first as indentation proceeds, the varying contrast

between $(\sigma_1^{AoS})_{pk}$ and $(\sigma_1^{CS})_{pk}$ shown above implies the dependence of fracture mode on the fracture strength. For the case with $E_c/E_s = 4.0$ and $\nu_c = \nu_s = 0.3$, Fig. 4a shows that if the normalized fracture strength is either sufficiently low or high, $(\sigma_1^{CS})_{pk}$ would reach the fracture strength first, therefore resulting in ring crack. The lower and upper thresholds of the normalized fracture strength for ring cracking can be readily determined from Fig. 4a to be around 0.05 and 0.9. Here normalized fracture strength is defined as $\bar{\sigma}_f \equiv \sigma_f \pi R / E_c^* t$. If $\bar{\sigma}_f < 0.05$ or $\bar{\sigma}_f > 0.9$ ring cracking occurs. Otherwise, radial cracking takes place. It should be noted that the lower and upper thresholds of the normalized fracture strength for ring/radial cracking are functions of modulus ratio $E_c/E_s$, and Poisson's ratios $\nu_c$ and $\nu_s$. Given $\nu_c$ and $\nu_s$, they are found to converge as $E_c/E_s$ decreases. There exists a critical value of $E_c/E_s$, at which they converge to one value. For the case of $\nu_c = \nu_s = 0.3$, this critical modulus ratio is found to be around 1.6, at which the evolution of the normalized $(\sigma_1^{CS})_{pk}$ and $(\sigma_1^{AoS})_{pk}$ is displayed in Fig. 4b. If $E_c/E_s$ is lower than this critical value, $(\sigma_1^{CS})_{pk}$ is always higher than $(\sigma_1^{AoS})_{pk}$ irrespective of the contact radius. In that case, ring cracking is expected to occur first irrespective of the value of $\bar{\sigma}_f$. Recalling the definition of the normalized fracture strength $\bar{\sigma}_f \equiv \sigma_f \pi R / E_c^* t$, the value of $\bar{\sigma}_f$ depends not only on the geometrical and mechanical properties of the laminated materials under indentation but also on the dimension of the indenter characterized by the tip radius $R$. If the modulus ratio $E_c/E_s$ is lower than the critical value mentioned above, the advent of ring cracking is ensured irrespective of the indenter radius. Such critical value of $E_c/E_s$ is therefore termed as the *critical modulus mismatch* (CMM) for ensuring ring cracking mode. For homogenous case with $E_c/E_s = 1.0$ and $\nu_c = \nu_s$, our results show that the maximum tensile stress always occurs on the coating
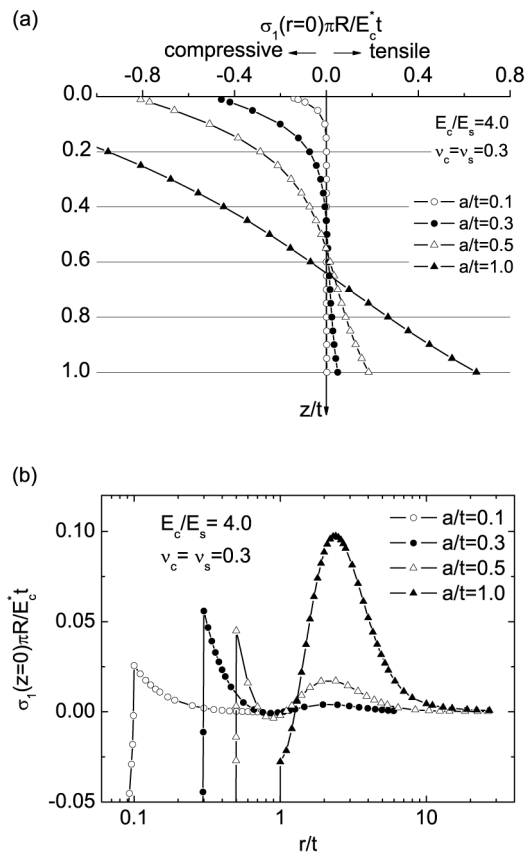
**Figure 3** | (a) Variation of the normalized maximum principal stress along the axis of symmetry ($r = 0$), and (b) coating surface ($z = 0$).

surface along the radial direction. Therefore, ring cracking, instead of radial cracking, occurs first for brittle materials. This conclusion is consistent with the prediction of the classic Hertzian theory[31].

**Fracture mode map.** The dependence of fracture mode on stiffness ratio $E_c/E_s$ and normalized fracture strength $\bar{\sigma}_f$ can be systematically depicted by a map in terms of these two nondimensional parameters, as shown in Fig. 5 for the case of $v_c = v_s = 0.3$. It can be seen that a v-shaped curve divides the plane into two regions corresponding to radial cracking and ring cracking respectively. The valley point of the v-shaped boundary corresponds to the scenario with CMM. It shows again that the destructive radical cracking can be inhibited or deferred for indenters of any size as long as the modulus ratio $E_c/E_s$ is lower than the CMM.

It should be pointed out that the CMM revealed above depends on the Poisson's ratios of both coating and substrate. To gain a deeper insight into the effect of Poisson's ratios on the CMM, we studied a series of cases with $v_c$ and $v_s$ in the reasonably broad range from 0.1 to 0.4. Fig. 6a shows the variation of CMM as a function of $v_c$ and $v_s$. It can be seen that CMM is proportional to $v_s$ while inversely proportional to $v_c$. Therefore, CMM reaches its maximum and minimum at $v_c = 0.1$, $v_s = 0.4$, and $v_c = 0.4$, $v_s = 0.1$ respectively. The corresponding maps of fracture mode for these two limiting cases are displayed in Fig. 6b. In comparison to the case with $v_c = v_s = 0.3$ shown in Fig. 5, it can be seen that the territory of radical cracking regime shrinks in the case of $v_c = 0.1$, $v_s = 0.4$ while expands in the case of $v_c = 0.4$, $v_s = 0.1$, resulting in CMMs equal to 3.3 and 1.0 respectively.

## Discussion

For the laminated biomaterials in nature, it may not be easy to obtain the precise Poisson's ratio for each layer and then to predict the
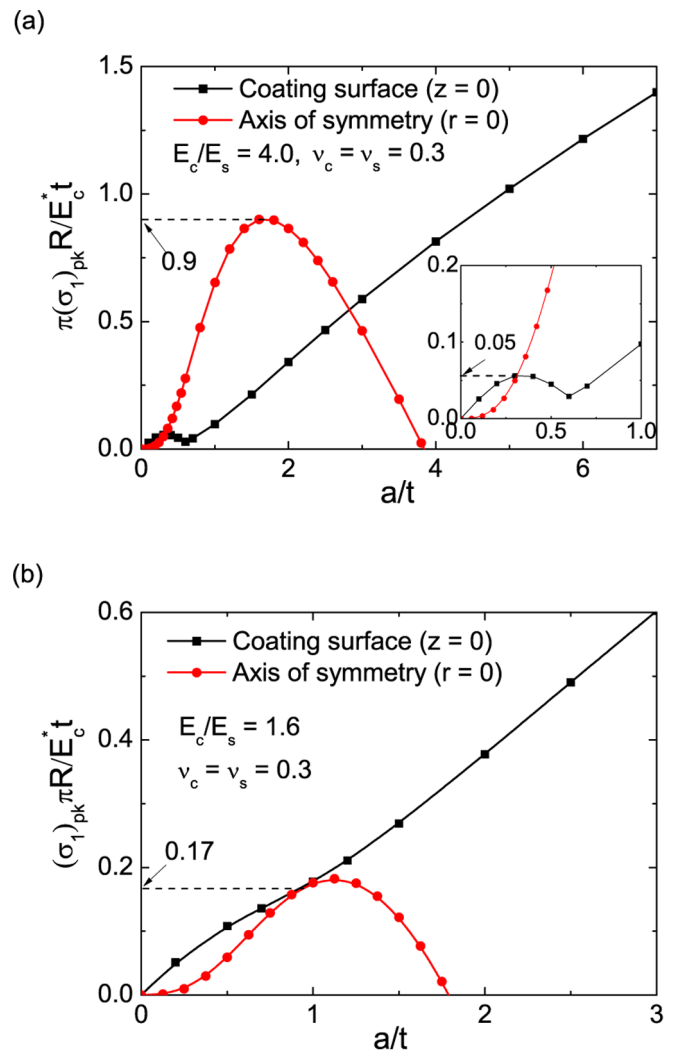


**Figure 4** | **Variation of the peak principal stresses on the coating surface and the axis of symmetry with the normalized contact radius for** (a) $E_c/E_s = 4.0$, $v_c = v_s = 0.3$, and (b) $E_c/E_s = 1.6$, $v_c = v_s = 0.3$.

corresponding CMM. However, if we take 0.1–0.4 as the reasonable range of Poisson's ratio of biomaterials, the CMM of natural laminated biomaterials, in the light of Fig. 6a, is estimated ranging from 1.0 to 3.3. It is interesting to compare this theoretical prediction with the measured value. Table 1 listed the modulus mismatch of some
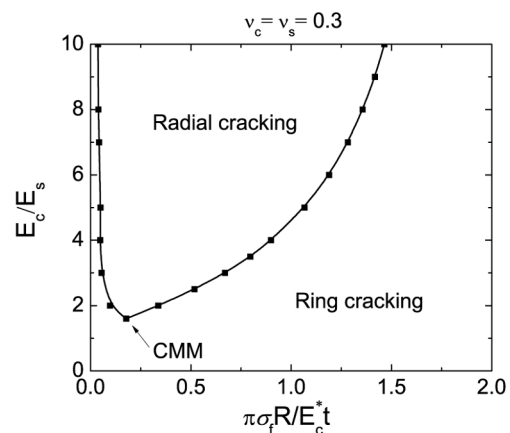


**Figure 5** | **Fracture mode map for case with Poisson's ratios $v_c = v_s = 0.3$.**
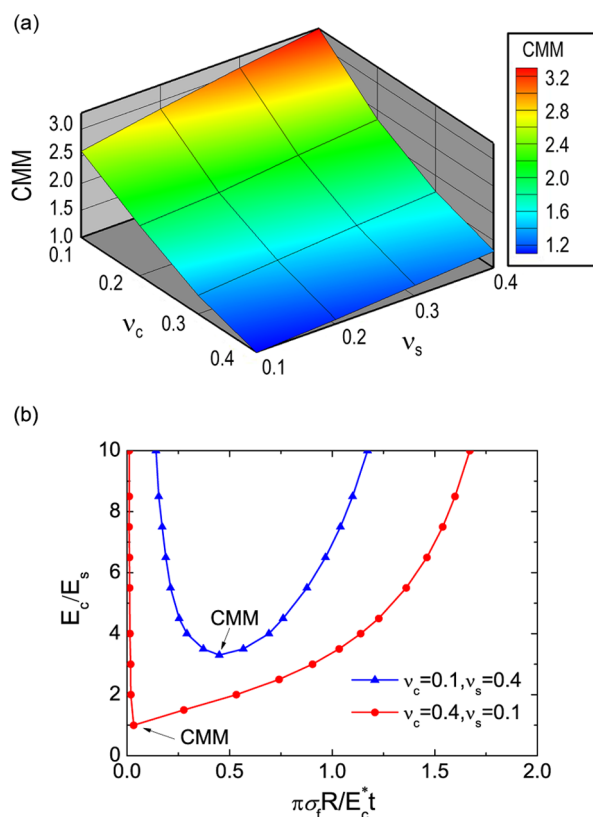
**Figure 6** | (a) Calculated CMM as function of Poisson's ratios $\nu_c$ and $\nu_s$ ranging from 0.1 to 0.4; (b) Fracture mode maps for the cases with the maximum and minimum CMMs in (a).

laminated biomaterials reported in literature. The inclination to ring cracking has been confirmed in some of these materials such as the scale of *Polypterus senegalus* being bitten by its predator's teeth[1]. It is interesting to notice that the measured modulus mismatch of the listed biomaterials range from 0.93 to 3.6, overlapping the range of the CMM calculated above. However, for a particular case such as the teeth of *Mylopharyngodon piceus*[19], if the Poisson's ratios of the coating (enameloid) and substrate (dentine) are both taken as 0.3, the CMM is estimated to be around 1.6, which is lower than the measured modulus mismatch 3.5 as shown in Table 1. Such discrepancy may result from our negligence of more specific features in our modeling above. For example, in our previous analysis, we assumed that the modulus across the coating/substrate interface is discontinuous. In fact, transitional interlayer with graded properties is often observed between distinct layers in natural laminated biomaterials.

Such gradient interlayer has been demonstrated to play an important role in mitigating the stress and strain concentration at the interface[1,18]. The effect of gradient transition layer on the CMM is studied by using finite element analysis (Supplementary Information). Fig. 7 shows the calculated fracture mode maps for the cases with gradient interlayer of thickness $t_{grad}$ in comparison to those without interlayer. It can be seen that the radial cracking regime shrinks and the CMM increases after introducing the gradient interlayer between the coating and substrate. The thicker the interlayer, the higher the CMM. For the teeth of *Mylopharyngodon piceus*, the reduced modulus obtained by nano-indentation exhibits gradient in the vicinity of the enameloid/dentine interface[19]. Assuming that the thickness of the gradient interlayer is equal to the coating (enameloid layer) thickness, Fig. 7 implies that the CMM could rise up to 3.5, which agrees well with its measured value.

From the perspective of ensuring ring cracking as the initial fracture mode, soft coating in combination with hard substrate seems more preferable. But why do natural materials barely adopt such kind of design? A conceivable answer to this question is because fracture mode may not be the only issue that biomaterials should tackle. Consideration of other issues such as strength, toughness, wear resistance and economics of construction and maintenance[32] may raise different and even competing requirements for the stiffness layout in different layers. The modulus mismatch in the existing biomaterials is most likely a consequence of optimization of diverse design requirements including fracture mode control.

Inspired by the inclination to ring cracking observed in most natural biomaterials, in this paper we theoretically explored the factors determining the emergence of radial cracking and ring cracking in coating/substrate systems. It was revealed that the fracture mode of the coating depends on the coating/substrate modulus mismatch and indenter size. There exists a critical modulus mismatch, CMM, below which emergence of ring cracking always precedes that of radical cracking irrespective of the indenter size. For structural materials, radial cracking is much more catastrophic in comparison to the ring one. Our results imply a strategy to inhibit catastrophic damage by controlling the modulus mismatch. For structural biomaterials in nature, the CMM was estimated to be in the range from 1.0 to 3.3, consistent with the values found in many existing structural biomaterials. Recalling the strengthening and toughening mechanisms discovered in biomaterials, it can be seen that structural biomaterials in nature utilize synergic strategies to mitigate damage due to external mechanical loadings at various intensities and length scales. If the load is relatively low, the intrinsic carrying capacity with the aid of diverse strengthening mechanisms prevents the onset of fracture. If the load exceeds the fracture strength and hence causes crack initiation, various toughening mechanisms operate and resist the subsequent growth of cracks. If indeed overwhelming load is encountered and partial or even whole structural damage is unavoid-

| Table 1 | The modulus mismatch of some laminated structural materials in nature |
|---|---|---|---|
| Laminated materials in nature | $E_c$ (GPa)* | $E_s$ (GPa)* | $E_c/E_s$ |
| Tooth of *M. Piceus* §(Black carp)[19] | ~70† | ~20† | ~3.5 |
| Shell of *C. squamiferum*[18] | ~28.8 | ~8.0 | ~3.6 |
| Shell of *Haliotis rufescens* (California red abalone)[33] | ~65† | ~70† | ~0.93 |
| Scale of *Arapaimas gigas*[34,35] | ~46.8‡ | ~16.7‡ | ~2.8 |
| | ~33.7Δ | ~15.7Δ | ~2.15 |
| Scale of *Polypterus senegalus*[1] | ~62 | ~29 | ~2.1 |
| Scale of *Morone saxatilis*[33] | ~1.0† | ~0.45† | ~2.2 |
| Exoskeleton of *Homarus americanus* (American Lobster)[36] | ~9.4& | ~6.6& | ~1.42 |

*Modulus here refers to, unless indicated otherwise, the reduced modulus obtained by nano-indentation;
§The occlusal surfaces of black carp teeth are flat and therefore laminated plate model is applicable;
†Young's modulus obtained by tensile tests;
‡Dehydrated samples;
ΔHydrated samples;
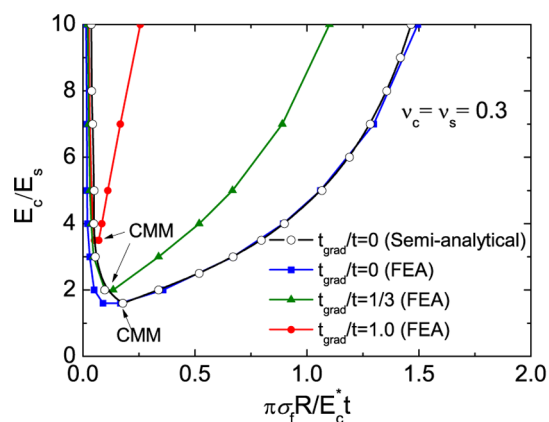&Mean value of the reduced moduli in normal and transverse directions.

**Figure 7 | Effect of gradient transition layer on the CMM.** In the gradient transition layer, the Young's modulus is assumed to vary from the modulus of the coating to that of the substrate in a linear way. Here $t_{grad}$ and $t$ stand for the thicknesses of gradient layer and coating respectively. Poisson's ratios are consistently taken as 0.3.

able, as the last resort, fracture mode may be controlled to inhibit or defer the catastrophic failure. It is the synergy of strengthening, toughening and fracture mode controlling that ensures higher survival probability of the structural biomaterials and their associated species in the intensive biological competitions. In summary, prevention of catastrophic structural failure is the most important goal of structural material design. Reducing the extent of overall structure damage caused by fracture is as important as strength and toughness to the safety and integrity of structures. Fracture mode control is one key strategy that we learned from natural biomaterials to combat catastrophic damage. Nevertheless, the existence of other mechanisms is expected and deserves further investigations.

1. Bruet, B. J., Song, J., Boyce, M. C. & Ortiz, C. Materials design principles of ancient fish armour. *Nat. Mater.* **7**, 748–756 (2008).
2. Ortiz, C. & Boyce, M. C. Bioinspired structural materials. *Science* **319**, 1053–1054 (2008).
3. Zhu, D. *et al.* Structure and mechanical performance of a "modern" fish scale. *Adv. Eng. Mater.* **14**, B185–B194 (2011).
4. Meyers, M. A., Lin, Y. S., Olevsky, E. A. & Chen, P.-Y. Battle in the amazon: Arapaima versus Piranha. *Adv. Eng. Mater.* **9**, B279–B288 (2012).
5. Gao, H., Ji, B., Jäger, I. L., Arzt, E. & Fratzl, P. Materials become insensitive to flaws at nanoscale: lessons from nature. *Proc. Natl. Acad. Sci. USA* **100**, 5597–5600 (2003).
6. Kolednik, O., Predan, J., Fischer, F. D. & Fratzl, P. Bioinspired design criteria for damage-resistant materials with periodically varying microstructure. *Adv. Funct. Mater.* **21**, 3634–3641 (2011).
7. Evans, A. G. *et al.* Model for the robust mechanical behavior of nacre. *J. Mater. Res.* **16**, 2475–2484 (2001).
8. Wang, R. Z., Suo, Z., Evans, A. G., Yao, N. & Aksay, I. A. Deformation mechanisms in nacre. *J. Mater. Res.* **16**, 2485–2493 (2001).
9. Zhang, Y., Yao, H., Ortiz, C., Xu, J. & Dao, M. Bio-inspired interfacial strengthening strategy through geometrically interlocking designs. *J. Mech. Behav. Biomed.* **15**, 70–77 (2012).
10. Jackson, A. P., Vincent, J. F. V. & Turner, R. M. The mechanical design of nacre. *Proc. Roy. Soc. Lond. B* **234**, 415–440 (1988).
11. Sarikaya, M., Gunnison, K. E., Yasrebi, M. & Aksay, J. A. Mechanical property-microstructural relationships in abalone shell. *Mater. Res. Soc.* **174**, 109–116 (1990).
12. Xie, Z. & Yao, H. Crack deflection and flaw tolerance in 'brick-and-mortar' structured composites. *Int. J. Appl. Mech.* **6**, 1450017 (2014).
13. Huang, Z. W. & Li, X. D. Origin of flaw-tolerance in nacre. *Sci. Rep.* **3**, 1693 (2013).
14. Bonderer, L. J., Studart, A. R. & Gauckler, L. J. Bioinspired design and assembly of platelet reinforced polymer films. *Science* **319**, 1069–1073 (2008).
15. Munch, E. *et al.* Tough, bio-inspired hybrid materials. *Science* **322,** 1516–1520 (2008).
16. Brandt, K., Wolff, M. F., Salikov, V., Heinrich, S. & Schneider, G. A. A novel method for a multi-level hierarchical composite with brick-and-mortar structure. *Sci. Rep.* **3**, 2322 (2013).
17. Cheng, Q., Wu, M., Li, M., Jiang, L. & Tang, Z. Ultratough artificial nacre based on conjugated cross-linked graphene oxide. *Angew. Chem. Int. Edit* **52**, 3750–3755 (2013).
18. Yao, H. *et al.* Protection mechanisms of the iron-plated armor of a deep-sea hydrothermal vent gastropod. *Proc. Natl. Acad. Sci. USA* **107**, 987–999 (2010).
19. He, C., Zhou, W., Wang, H., Shi, S.-Q. & Yao, H. Mechanics of pharyngeal teeth of black carp (Mylopharyngodon piceus) crushing mollusk shells. *Adv. Eng. Mater.* **15**, 684–690 (2013).
20. Chai, H., Lawn, B. & Wuttiphan, S. Fracture modes in brittle coatings with large interlayer modulus mismatch. *J. Mater. Res.* **14**, 3805–3817 (1999).
21. Du, J., Niu, X., Rahbar, N. & Soboyejo, W. Bio-inspired dental multilayers: effects of layer architecture on the contact-induced deformation. *Acta Biomater.* **9**, 5273–5279 (2013).
22. Meyers, M. A. & Chawla, K. K. *Mechanical Behavior of Materials* (Cambridge University Press, New York, 2008).
23. Rankine, W. J. M. On the stability of loose earth. *Phil. Trans. R. Soc. Lond.* **147**, 9–27 (1857).
24. Barthel, E. & Perriot, A. Adhesive contact to a coated elastic substrate. *J. Phys. D: Appl. Phys.* **40**, 1059–1067 (2007).
25. Nogi, T. & Kato, T. Influence of a hard surface layer on the limit of elastic contact. Part I: Analysis using a real surface mode. *ASME J. Trib.* **119**, 493–500 (1977).
26. Li, J. & Chou, T.-W. Elastic filed of a thin-film/substrate system under an axisymmetric loading. *Int. J. Solids Struct.* **34**, 4463–4478 (1997).
27. Perriot, A. & Barthel, E. Elastic contact to a coated half-space: Effective elastic modulus and real penetration. *J. Mat. Res.* **19**, 600–608 (2004).
28. Mary, P., Chateauminois, A. & Fretigny, C. Deformation of elastic coatings in adhesive contacts with spherical probes. *J. Phys. D: Appl. Phys.* **39**, 3665–3673 (2006).
29. Suresh, S., Giannakopoulos, A. E. & Alcala, J. Spherical indentation of compositionally graded materials: theory and experiments. *Acta Mater.* **45**, 1307–1321 (1997).
30. Jitcharoen, J., Padture, N. P., Giannakopoulos, A. E. & Suresh, S. Hertzian-crack supression in ceramics with elastic-modulus-graded surfaces. *J. Am. Ceram. Soc.* **81**, 2301–2308 (1998).
31. Johnson, K. L. *Contact Mechanics* 94 (Cambridge University Press, Cambridge, 1985).
32. Vermeij, G. J. The economics of construction and maintenance in *A Natural History of Shells* 39–58 (Princeton University Press, 1993).
33. Li, X., Chang, W.-C., Chao, Y. J., Wang, R. Z. & Chang, M. Nanoscale structural and mechanical characterization of a natural nanocomposite material: the shell of red abalone. *Nano Letters* **4**, 613–617 (2004).
34. Lin, Y. S., Wei, C. T., Olevsky, E. A. & Meyers, M. A. Mechanical properties and the laminate structure of Arapaima gigas scales. *J Mech Behav Biomed Mater* **4**, 1145–1156 (2011).
35. Chen, P. Y. *et al.* Predation versus protection: Fish teeth and scales evaluated by nanoindentation. *J. Mater. Res.* **27**, 100–112 (2012).
36. Sachs, C., Fabritius, H. & Raabe, D. Hardness and elastic properties of dehydrated cuticle from the lobster Homarus americanus obtained by nanoindentation. *J. Mater. Res.* **21**, 1987–1995 (2006).

## Acknowledgments

## Author contributions

H.Y. developed the concept, conceived the study and conducted the theoretical analysis. Z.X. performed the finite element simulations. Z.X. and C.H. carried out indentation test. H.Y. and M.D. discussed the results and wrote the manuscript. H.Y. supervised the work.

## Additional information

1  **Supporting Information**

2  **Fracture mode control: a bio-inspired strategy to combat catastrophic**
3  **damage**

4  Haimin Yao[a,1], Zhaoqian Xie[a], Chong He[a], Ming Dao[b]

5  [a] Department of Mechanical Engineering, the Hong Kong Polytechnic University, Hung

6  Hom, Kowloon, Hong Kong

7  [b] Department of Materials Science and Engineering, Massachusetts Institute of

8  Technology, Cambridge, MA 02139, USA

9

10  **Semi-analytical solution to the stress field**

11  The contact problem posed in Fig. 2a has been systematically studied in the framework of

12  elasticity theory. The initial analytical investigation can date back to 1997 when Li and

13  Chou[1] and Nogiand Kato[2] independently established the Green function for the coated

14  elastic substrate. Based on their work, Perriot and Barthel[3] reformulated the problem by

15  introducing two cosine Fourier transform-based auxiliary functions, which enable the

16  problem to be solved at lower numerical cost. Subsequent extension from Hertzian

17  (non-adhesive) contact to adhesive contact was made by Mary *et al.*[4] and Barthel and

18  Perriot[5].

19      To predict the fracture mode on the basis of the Rankine criterion, the knowledge of

20  the maximum principal stress $\sigma_1$ especially its peak value(s) and occurring location(s) is

21  necessary. Although it is difficult the obtain the analytical solution to the field of $\sigma_1$,

22  previous solutions in literature implies that the field of $\sigma_1$ exhibits two local peaks

23  occurring at the coating surface ($z = 0$) and axis of symmetry ($r = 0$) respectively[6]. Such

24  feature in the spacial distribution of $\sigma_1$ can be readily confirmed by finite element

25  analysis. Moreover, radial direction is found to be the principal direction of $\sigma_1$ on the

26  coating surface and axis of symmetry. Therefore, the peaks of $\sigma_1$ are equal to the

27  maximum radial stress $\sigma_r$ along the coating surface and the axis of symmetry

28  respectively; so that we just need to focus our attention on the solution to the radial stress

29  $\sigma_r$.

---

[1] To whom correspondence may be addressed. E-mail: mmhyao@polyu.edu.hk (H. Yao)

30    Referring to the existing theory of contact mechanics[7], the radial stress developed in

31    the coating can be expressed in terms of Hankel transforms as follows

32    $$\sigma_r(r,z) = \mathcal{H}_0[Y_c(\xi,z);\xi \to r] - \frac{2G_c}{r}\mathcal{H}_1[U_c(\xi,z);\xi \to r] \tag{1}$$

33    where $\mathcal{H}_0$ and $\mathcal{H}_1$ denote the Hankel transforms of order 0 and 1 respectively and

34    functions

35    $$Y_c(\xi,z) = (\xi z A_c - 2\nu_c A_c + C_c)e^{-\xi z} + (2\nu_c B_c + \xi z B_c + D_c)e^{\xi z} \tag{2a}$$

36    $$U_c(\xi,z) = \frac{(\xi z A_c + C_c)\xi^{-1}e^{-\xi z} + (\xi z B_c + D_c)\xi^{-1}e^{\xi z}}{2G_c} \tag{2b}$$

37    with $G_c$, $\nu_c$ denoting the shear modulus and Poisson's ratio of the coating and $A_c(\xi)$,

38    $B_c(\xi)$, $C_c(\xi)$ and $D_c(\xi)$ being four functions of $\xi$ to be determined. By taking

39    advantage of the boundary conditions of the posed problem, it can be demonstrated that

40    these unknown functions are correlated and there is only one independent function among

41    them. Without loss of generality, $A_c$ is chosen as the independent function and the other

42    three can be expressed in terms of $A_c$ as follows:

43    $$B_c = \frac{b_0[(1+2t\xi)e^{2t\xi} - a_0]}{e^{4t\xi} + b_0(2t\xi - 1)e^{2t\xi}}A_c \tag{3a}$$

44    $$D_c = \frac{(\kappa_c - 2t\xi)}{2}B_c - \frac{a_0}{2}e^{-2t\xi}A_c \tag{3b}$$

45    $$C_c = D_c - (1 - 2\nu_c)(A_c + B_c) \tag{3c}$$

46    where $t$ denotes the coating thickness and $a_0 \equiv \frac{\alpha\kappa_s - \kappa_c}{(\alpha\kappa_s + 1)}$, $b_0 \equiv \frac{\alpha - 1}{(\alpha + \kappa_c)}$,

47    $\alpha \equiv G_c/G_s$, $\kappa_c \equiv 3 - 4\nu_c$ and $\kappa_s \equiv 3 - 4\nu_s$ are non-dimensional constants associated with

48    the mechanical properties of the coating and substrate. Besides, function $A_c(\xi)$ is

49    demonstrated to be correlated with the pressure applied on the coating surface $p(r)$

50    through

51    $$A_c(\xi) = \frac{1 + b_0(2t\xi - 1)e^{-2t\xi}}{1 - [b_0 + a_0 + 4b_0 t^2\xi^2]e^{-2t\xi} + a_0 b_0 e^{-4t\xi}}\tilde{p}(\xi) \tag{4}$$

52  where $\tilde{p}(\xi)$ is the Hankel transforms of order 0 of $p(r)$ defined by

53  $\tilde{p}(\xi) = \int_0^\infty rp(r)J_0(r\xi)dr$ with $J_0(\cdot)$ denoting the Bessel Function of the first kind of

54  order 0. However, solving $A_c(\xi)$ through Eq. (4) is still difficult due to the mixed

55  boundary condition on the coating surface in this problem. To tackle this problem,

56  Barthel and coworkers[8, 9] ingeniously introduced an auxiliary function $g(s)$, the cosine

57  Fourier transform of function $\tilde{p}(\xi)$ defined by

58  $$g(s) = \int_0^\infty \tilde{p}(\xi)\cos(\xi s)d\xi \qquad (s \le a) \tag{5}$$

59  and established an integral equation with respect to $g(s)$ which, for Hertzian

60  (non-adhesive) contact, is given by

61  $$\frac{a^2 - s^2}{R} = \frac{2}{E_c^*}\left[ g(s) + \int_0^a \Delta K(\rho, s)g(\rho)d\rho \right] \quad (s \le a) \tag{6}$$

62  where $a$ denotes the radius of the contact region, $E_c^* \equiv E_c /(1 - v_c^2)$ with $E_c$ and $v_c$

63  being the Young's modulus and Poisson's ratio of the coating respectively, and

64  $$\Delta K(\rho, s) = K(\rho, s) - K(\rho, a) \tag{7a}$$

65  $$K(\rho, s) = \frac{2}{\pi}\int_0^\infty \frac{(b_0 + a_0 + 4b_0 t^2 \xi^2 + 4b_0 t\xi)e^{-2t\xi} - 2a_0 b_0 e^{-4t\xi}}{1 - (b_0 + a_0 + 4b_0 t^2 \xi^2)e^{-2t\xi} + a_0 b_0 e^{-4t\xi}}\cos(\xi s)\cos(\xi\rho)d\xi \tag{7b}$$

66  Using the coating thickness $t$ as the characteristic length scale for normalization, Eqs. (6)

67  and (7) can be normalized to be

68  $$\bar{a}^2 - \bar{s}^2 = \bar{g}(\bar{s}) + \int_0^{\bar{a}} \Delta\bar{K}(\bar{\rho}, \bar{s})\bar{g}(\bar{\rho})d\bar{\rho} \qquad (\bar{s} \le \bar{a}) \tag{8}$$

69  $$\Delta\bar{K}(\bar{\rho}, \bar{s}) = t\Delta K(\rho, s) = \bar{K}(\bar{\rho}, \bar{s}) - \bar{K}(\bar{\rho}, \bar{a})$$

70  $$\bar{K}(\bar{\rho}, \bar{s}) = \frac{2}{\pi}\int_0^\infty \frac{(b_0 + a_0 + 4b_0\bar{\xi}^2 + 4b_0\bar{\xi})e^{-2\bar{\xi}} - 2a_0 b_0 e^{-4\bar{\xi}}}{1 - (b_0 + a_0 + 4b_0\bar{\xi}^2)e^{-2\bar{\xi}} + a_0 b_0 e^{-4\bar{\xi}}}\cos(\bar{\xi}\bar{s})\cos(\bar{\xi}\bar{\rho})d\bar{\xi}$$

71  where $\bar{a} = a/t, \bar{\rho} = \rho/t, \bar{s} = s/t$, $\bar{g}(\bar{s}) = g(s)/\left(\dfrac{E_c^* t^2}{2R}\right)$, $\bar{\xi} = \xi t$. Subsequently, the

72  normalized $\tilde{p}(\xi)$ and $A_c(\xi)$ are given by

3

73
$$\overline{\overline{p}}(\overline{\xi}) = \tilde{p}(\xi) \bigg/ \left( \frac{E_c^* t^3}{\pi R} \right) = \int_0^{\overline{a}} \overline{g}(\overline{s}) \cos(\overline{\xi}\overline{s}) d\overline{s}$$
(9)

74
$$\overline{A}_c(\overline{\xi}) = A_c(\xi) \bigg/ \left( \frac{E_c^* t^3}{\pi R} \right) = \overline{\overline{p}}(\overline{\xi}) \frac{1 + b_0(2\overline{\xi} - 1)e^{-2\overline{\xi}}}{1 - [b_0 + a_0 + 4b_0\overline{\xi}^2]e^{-2\overline{\xi}} + a_0 b_0 e^{-4\overline{\xi}}}$$
(10)

75 Then, the normalized form of other functions $B_c$, $C_c$, and $D_c$ can be given by

76
$$\overline{B}_c(\overline{\xi}) = B_c \bigg/ \left( \frac{E_c^* t^3}{\pi R} \right) = \frac{b_0[(1 + 2\overline{\xi})e^{2\overline{\xi}} - a_0]}{e^{4\overline{\xi}} + b_0(2\overline{\xi} - 1)e^{2\overline{\xi}}} \overline{A}_c$$
(11)

77
$$\overline{D}_c(\overline{\xi}) = D_c \bigg/ \left( \frac{E_c^* t^3}{\pi R} \right) = \frac{(\kappa_c - 2\overline{\xi})}{2} \overline{B}_c - \frac{a_0}{2} e^{-2\overline{\xi}} \overline{A}_c$$
(12)

78
$$\overline{C}_c(\overline{\xi}) = C_c \bigg/ \left( \frac{E_c^* t^3}{\pi R} \right) = \overline{D}_c - (1 - 2\nu_c)(\overline{A}_c + \overline{B}_c)$$
(13)

79 The normalized radial stress can be given by

80
$$\overline{\sigma}_r(\overline{r}, \overline{z}) = \sigma_r(r, z) \bigg/ \left( \frac{E_c^* t}{\pi R} \right) = \mathcal{H}_0[\overline{Y}_c(\overline{\xi}, \overline{z}); \overline{\xi} \to \overline{r}] - \frac{1}{\overline{r}} \mathcal{H}_1[\overline{U}_c(\overline{\xi}, \overline{z}); \overline{\xi} \to \overline{r}]$$
(14)

81 where

82
$$\overline{Y}_c(\overline{\xi}, \overline{z}) = Y_c \bigg/ \left( \frac{E_c^* t^3}{\pi R} \right) = (-2\nu_c \overline{A}_c + \overline{\xi}\overline{z}\overline{A}_c + \overline{C}_c)e^{-\overline{\xi}\overline{z}} + (2\nu_c \overline{B}_c + \overline{\xi}\overline{z}\overline{B}_c + \overline{D}_c)e^{\overline{\xi}\overline{z}}$$
(15a)

83
$$\overline{U}_c(\overline{\xi}, \overline{z}) = U_c \bigg/ \left( \frac{E_c^* t^4}{2G_c \pi R} \right) = (\overline{\xi}\overline{z}\overline{A}_c + \overline{C}_c)\overline{\xi}^{-1}e^{-\overline{\xi}\overline{z}} + (\overline{\xi}\overline{z}\overline{B}_c + \overline{D}_c)\overline{\xi}^{-1}e^{\overline{\xi}\overline{z}}$$
(15b)

84
$$\overline{Z}_c(\overline{\xi}, \overline{z}) = Z_c \bigg/ \left( \frac{E_c^* t^3}{\pi R} \right) = -2\nu_c \overline{A}_c e^{-\overline{\xi}\overline{z}} + 2\nu_c \overline{B}_c e^{\overline{\xi}\overline{z}}$$
(15c)

85

86     Although Eq. (14) gives the expression of the normalized radial stress, it involves
87 Hankel transforms of complicated functions which cannot be accomplished analytically.
88 Numerical approach has to be applied to obtain the normalized radial stress field. In this
89 regards, the obtained result is termed "semi-analytical" solution.

4

90        From above formulation, it can be seen that the influence of the mechanical

91     properties on the stress is exerted through parameters $a_0$, $b_0$, $\alpha$, $\kappa_c$ and $\kappa_s$, which are

92     functions of three independent dimensionless constants $\dfrac{E_c}{E_s}$, $\nu_c$ and $\nu_s$. From Eq.

93     (14), it can be noticed that the radial stress in coating can be expressed in terms of

94     $\dfrac{E_c^* t}{\pi R} \cdot \bar{\sigma}_r(\bar{r}, \bar{z}, \dfrac{E_c}{E_s}, \nu_c, \nu_s, \bar{a})$, where the normalized radial stress $\bar{\sigma}_r(\bar{r}, \bar{z}, \dfrac{E_c}{E_s}, \nu_c, \nu_s, \bar{a})$ is a

95     dimensionless function of normalized coordinates $\bar{r}$ and $\bar{z}$, mechanical properties

96     characterized by $\dfrac{E_c}{E_s}$, $\nu_c$ and $\nu_s$, and the normalized contact radius $\bar{a}$. Given $\bar{r}, \bar{z}$,

97     $\dfrac{E_c}{E_s}$, $\nu_c$, $\nu_s$, the normalized radial stress can be calculated numerically by following a

98     procedure as follows. First, function $\bar{g}(\bar{s})$ is determined numerically by solving the

99     integral equation of Eq.(8). Then function $\bar{\bar{p}}(\xi)$ is obtained by taking the inversion of

100     cosine transform of function $\bar{g}(s)$ as shown in Eq. (9), followed by the determination of

101     function $\bar{A}_c(\xi)$ and its dependents $\bar{B}_c(\xi)$, $\bar{D}_c(\xi)$ and $\bar{C}_c(\xi)$ through Eqs. (10-13).

102     Finally, the normalized radial stress $\bar{\sigma}_r(\bar{r}, \bar{z})$ is determined based on Eqs. (14-15). The

103     whole solving procedure is graphically shown in Fig. S1.

$$\boxed{\bar{r}, \bar{z}, E_c / E_s, \nu_c, \nu_s, \bar{a}}$$

$$\downarrow$$

$$\boxed{\begin{array}{c}\text{Solve Eq. (8) for} \\ \bar{g}(\bar{s})\end{array}}$$

$$\downarrow$$

$$\boxed{\begin{array}{c}\text{Use Eq. (9) to} \\ \text{calculate } \bar{\bar{p}}(\xi)\end{array}}$$

$$\downarrow$$

$$\boxed{\begin{array}{c}\text{Use Eqs. (10-13) to get} \\ \bar{A}_c, \bar{B}_c, \bar{D}_c, \bar{C}_c\end{array}}$$

$$\downarrow$$

$$\boxed{\begin{array}{c}\text{Use Eqs. (14-15)} \\ \text{to get } \bar{\sigma}_r(\bar{r}, \bar{z})\end{array}}$$
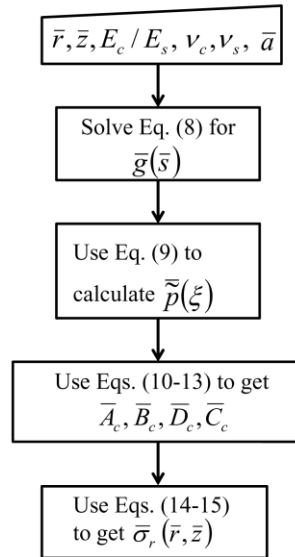
104

105     Figure S1 | Flow chart of the numerical approach to calculate the normalized radial stress.

**FEA analysis of the effect of gradient interlayer on CMM**
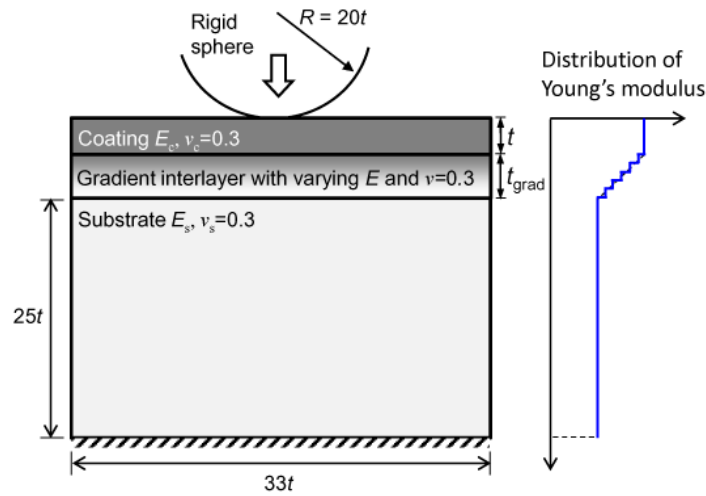


107

108            Figure S2 | Schematics of the FEA model for studying the effect of gradient

109                                            interlayer on fracture modes.

110    If a gradient interlayer is present between the coating and substrate, the problem may not

111    be able to be solved by analytical or semi-analytical approach as shown above. Finite

112    element analysis(FEA) has to be adopted to calculate the principal stress particularly its

113    peaks on the CS and AoS so as to predict the fracture modes. Fig. S2 shows the

114    schematics of the FEA model we used, in which a rigid spherical indenter is compressed

115    by external loading against a laminated material. Unlike the bilayer semi-analytical

116    model shown in Fig. 2, an additional gradient interlayer of thickness $t_{grad}$ is introduced

117    between the coating and substrate. The interfaces between different layers are assumed

118    perfectly bonded. The width and thickness of the substrate are taken as 33 and 25 times

119    of the coating thickness $t$ respectively, which are demonstrated large enough to eliminate

120    the boundary effect. The elastic gradient in the transition interlayer is achieved by

121    dividing it into 5 sub-layers, whose Young's moduli are taken as the values determined

122    by linear interpolation in accordance to its distances to the coating and substrate. The

123    Poisson's ratio in the whole model is uniformly taken as 0.3. The contact between

124    indenter and coating is assumed frictionless. Given modulus ratio $E_c/E_s$ between coating

125    and substrate, the indentation problem is simulated with commercial FEA software

126    ABAQUS (Dassault Systèmes) by using 4-node bilinear axisymmetric quadrilateral solid

127    element (CAX4R in ABAQUS). Sufficiently fine meshing is taken to ensure the mesh

128 convergence of the results. The evolution of the peaks of the principal stress on CS and

129 AoS with the contact size is obtained. By comparing the obtained peaks of the principal

130 stress with the fracture strength of the material, the condition for radical cracking and

131 ring cracking is obtained in terms of normalized fracture strength $\bar{\sigma}_f \equiv \sigma_f \pi R / E_c^* t$. Such

132 procedure is repeated for a series modulus ratio $E_c/E_s$. A fracture modes map then is

133 obtained as we did in the case without gradient interlayer. The effect of gradient

134 interlayer thickness $t_{grad}$ on the fracture modes is studied by taking $t_{grad}=0$, $t/3$ and $t$

135 respectively. The results are shown in Fig. 7 in comparison to that obtained by the

136 semi-analytical approach for the case without gradient interlayer.

137
138
139 **References:**
140 1.  Li J, Chou T-W. Elastic filed of a thin-film/substrate system under an
141       axisymmetric loading. *Int J Solids Struct* **34**, 4463-4478 (1997).
142 2.  Nogi T, Kato T. Influence of a hard surface layer on the limit of elastic contact.
143       Part I: Analysis using a real surface mode. *ASME J Trib* **119**, 493-500 (1977).
144 3.  Perriot A, Barthel E. Elastic contact to a coated half-space: Effective elastic
145       modulus and real penetration. *J Mat Res* **19**, 600-608 (2004).
146 4.  Mary P, Chateauminois A, Fretigny C. Deformation of elastic coatings in
147       adhesive contacts with spherical probes. *Journal of Physics D: Applied Physics* **39**,
148       3665-3673 (2006).
149 5.  Barthel E, Perriot A. Adhesive contact to a coated elastic substrate. *J Phys D:*
150       *Appl Phys* **40**, 1059-1067 (2007).
151 6.  Chai H, Lawn B, Wuttiphan S. Fracture modes in brittle coatings with large
152       interlayer modulus mismatch. *Journal of Materials Research* **14**, 3805-3817
153       (1999).
154 7.  Gladwell GM. *Contact Problem in the Classical Theory of Elasticity*. Sijthoff &
155       Noordhoff (1980).
156 8.  Huguet AS, Barthel E. Surface forces and the adhesive contact of axisymmetric
157       elastic bodies. *J Adhes* **74**, 143-175 (2000).
158 9.  Barthel E, Haiat G. Approximate model for the adhesive contact of viscoelastic
159       spheres. *Langmuir* **18**, 9362–9370 (2002).
160
161